MDPI

Article

Pore Characteristics and Influencing Factors of Marine and Lacustrine Shale in the Eastern Sichuan Basin, China

Jianglin He [1,2,]*, Lixia Zhu [1,2], Ankun Zhao [1,2], Dong Wang [1,2], Zhen Qiu [3] and Ping Yang [1,2]

1 Chengdu Center of Geological Survey, China Geological Survey, Chengdu 610082, China
2 Key Laboratory for Sedimentary Basin and Oil and Gas Resources, Ministry of Natural Resources, Chengdu 610081, China
3 PetroChina Research Institute of Petroleum Exploration and Development, China National Petroleum Corporation, Beijing 100083, China
* Correspondence: 5hjl998@163.com

Abstract: Although almost all the shale gas in China is exploited from marine shale (Wufeng–Longmaxi Formation) in Sichuan Basin and several prolific wells, it has also been obtained in Jurassic lacustrine shale. However, the reservoir conditions of the lacustrine shale are not well understood, which has impeded a breakthrough regarding lacustrine shale gas in Sichuan Basin. To probe the reservoir conditions of the lacustrine shale in Sichuan Basin, we take the Wufeng–Longmaxi shale and Dongyuemiao shale sampled from wells and outcrops as examples. A series of experiments were conducted, including TOC, XRD, FE-SEM, N_2 adsorption, Micro-CT, vitrinite reflectance and bitumen reflectance. The results show that the pores in marine shale are mainly composed of organic-matter-hosted pores (OM pores). However, in the lacustrine shale, the pores are mainly composed of dissolution pores and intergranular pores. The marine shale is characterized by small-caliber and large-volume pores in which cluster pores are levitated in the shale as kites and connected by past channels. However, in the lacustrine shale, the cluster pores and the past channels are mainly arranged according to the flow channels in the vertical direction. The arrangement of the pores in the marine shale is obviously deformed by compaction. The lacustrine shale is characterized by under-compaction. It can be deduced that the sweet spots for lacustrine shale gas are likely located at the areas characterized by under-compaction resulting from fluid pressure conducted upward, such as the hinge zone of syncline or the core of anticline overlap on the gas reservoirs.

Keywords: shale gas; pore structure; marine shale; lacustrine shale; shale reservoirs

1. Introduction

Shale gas, as an alternative resource awaiting exploitation, has received much attention for its large reserves [1]. Marine shale gas and terrestrial shale gas have been successfully developed in North America and China [2]. In China, shale gas exploration began in 2005 [3]. Up to 2021, the annual output of shale gas has amounted to 230×10^8 m^3 in China [4], which is the world's second most. Meanwhile, more than 90% of the shale gas was derived from Sichuan Basin [5,6] (Figure 1a). The Fuling shale gas field is also located in Eastern Sichuan Basin (Figure 1b), which is the largest shale gas field outside North America [7]. Up to now, almost all the shale gas from Sichuan Basin has been exploited from marine shale (Wufeng–Longmaxi Formation) [5]. However, with the development of shale gas, most of the unexploited marine shale gas is buried deeper than 3500 m in Sichuan Basin. A major challenge is being faced to maintain the increase in shale gas production in China because of more and more expensive [8] and harsh technical requirements for the hydraulic fracturing of deep shale gas (burial depth > 3500 m).

Since 2011, some authors have been focused on the lacustrine shale gas exploration in Sichuan Basin [9,10]. Up to now, industrial shale gas flow has been obtained in some areas of Sichuan Basin, such as Fuling [10,11], Yuanba [9] and Pingchang [12]. Several

prolific wells ($>20 \times 10^4$ m^3/d) were discovered in the Jurassic lacustrine shale. Especially, the daily production of well YL-21 is 50.9×10^4 m^3/d [13], whose commercial value is comparable to a marine shale gas well. Previous studies deduced that the area is about 4×10^4 km^2 [14], favorable for lacustrine shale gas exploration in Sichuan Basin. The Jurassic lacustrine shale has seemed to be a key player for increasing the shale gas and oil production in Sichuan Basin in the next several years [15]. However, the practices show that the large resource (10×10^8 t to 16×10^8 t) is not matching the small geological reserves of shale gas and oil (up to now, merely 0.8×10^8 t has been demonstrated) in the lacustrine shale. The poor reservoir properties are not matching the relatively high production of oil and gas [15]. These factors indicate that the reservoir conditions of the lacustrine shale have not been well understood, which has impeded obtaining a breakthrough regarding lacustrine shale gas in Sichuan Basin [15].
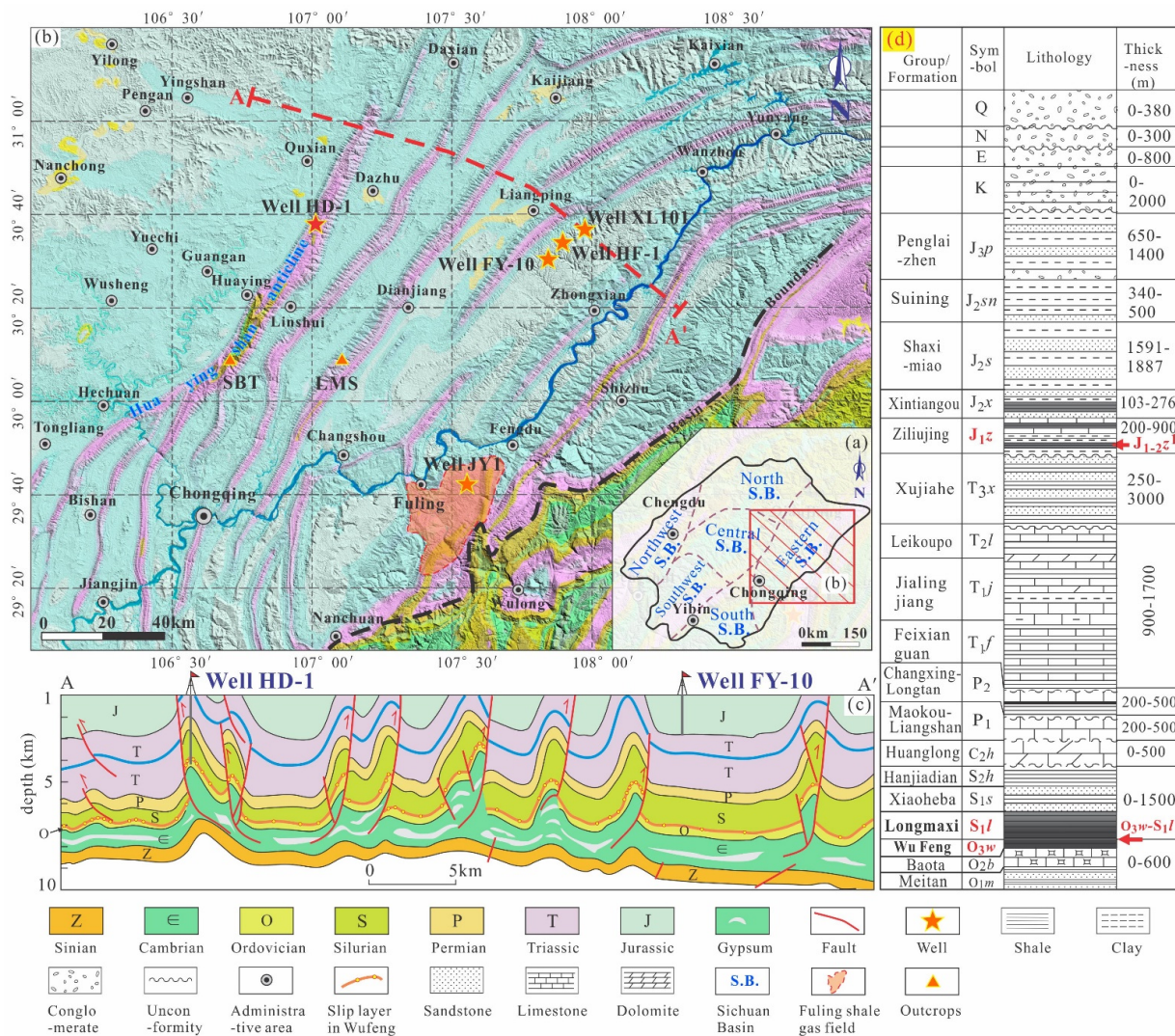
Figure 1. Geological overview of Sichuan Basin and the distribution of the study area. (**a**) The shape and structure units of Sichuan Basin. (**b**) Map of the Eastern Sichuan Basin showing the geomorphological features in the study area and the location of wells and outcrops. (**c**) The structural profile of Eastern Sichuan Basin showing the structure style and the location of well HD-1 and well FY-10. (**d**) Stratigraphic column of Eastern Sichuan Basin showing the vertical configuration relationship between marine and lacustrine shale.

In this work, based on geochemical, mineral, imaging and physical tests, we compared the difference of pore characteristics and influencing factors for marine shale (Wufeng–

Longmaxi shale) and lacustrine shale (Dongyuemiao shale) in the Eastern Sichuan Basin (Figure 1d), where industrial shale flow has been achieved both in marine and lacustrine shale. The pore characteristics and influencing factors will be considered, such as the formation mechanism, spatial arrangement and tectonic evolution of the pores, with an aim to probe the reservoir conditions of the lacustrine shale in Sichuan Basin. This research is expected to provide a useful reference for the commercial development of lacustrine shale gas in Sichuan Basin.

2. Geological Setting

Sichuan Basin is located on the western margin of Yangtze Craton in southwestern China [16], which covers an area of 180,000 km^2 [17]. Sichuan Basin comprises a 6000 to 12,000 m thick [18] Ediacaran to Cenozoic sedimentary succession overlying the pre-Sinian Proterozoic basement (Figure 1d). According to the difference in tectonic evolution of various regions in Sichuan Basin, it can be divided into the Eastern Sichuan Basin, the North Sichuan Basin, the Western Sichuan Basin, the Central Sichuan Basin, the Southwestern Sichuan Basin, and the Northwest Sichuan Basin (Figure 1a) [4]. The Eastern Sichuan Basin is a prominent Mesozoic NE-trending fold-and-thrust belt [9], where the high and steep structural zones were formed dominated by the intense compressing and thrusting force during later Yanshan Movement and Himalayan movement (Figure 1b,c) [19]. In the Eastern Sichuan Basin, the synclines are wider than the anticlines and are flat-bottomed [20].

Sichuan Basin has experienced a complex tectonic and sedimentary history since the breakup of Rodinia at approximately 750 Ma [21]. It consists of four main stages: (1) the Neoproterozoic rift stage (750–635 Ma), (2) the passive continental margin stage (635–488 Ma), (3) the Proto-Tethys ocean closure stage (488–420 Ma) and (4) the Orogeny stage (420 Ma to present) [22]. During the late Ordovician to early Silurian period, the Wufeng–Longmaxi Formation was deposited as the Middle-Upper Yangtze evolved into a shallow restricted basin [23,24] and a huge and thick marine shale was deposited in the deep inner shelf basin [24], which is the key production layer of shale gas in China now [22]. As the upper Yangtze collided with the Tethys block or the arc-basin collisional zone to the west [25] during the late Triassic to early Jurassic, Sichuan Basin was dominated by shores, shallow lakes and semi-deep lake facies during the early Jurassic period [26]. The Ziliujing Formation was deposited in this period, which is 200–900 m thick (Figure 1d) and consisted of Zhenzhuchong (J_1z), Dongyuemiao ($J_{1–2}z^1$), Ma'anshan ($J_{1–2}z^2$) and Da'anzhai ($J_{1–2}z^3$) members in the ascending stratigraphic order [27]. The maximum flooding surface in the early Jurassic period occurred in the middle part of the Dongyuemiao member [18]. The area of the lacustrine shales in Ziliujing Formation is around 78,000 km^2 [14] in Sichuan Basin.

3. Sample and Methods

3.1. Samples

In this work, both the core samples and outcrops data are taken into consideration to evaluate the influence of weathering action. The marine shale samples are both collected from the well HD-1 and SBT outcrops (Figure 1b). Previous studies have reported a great deal of test data of core samples from lacustrine shale, which are available for comparative study. The lacustrine shale samples were mainly collected from the LMS outcrops (Figure 1b), which are excavated more than 2 m under the surface. As shown in Tables 1 and 2, 55 samples were collected for TOC and XRD testing; 19 marine shale samples were collected for bitumen reflectance test, and 10 lacustrine samples were collected for vitrinite reflectance test. Further, 55 samples were collected for porosity and permeability test, but merely 35 samples were tested successfully; 41 samples were collected for N$_2$ adsorption test. According to the porosity test results, the samples HD1-17, SBT-R10 and LMS-T9 were collected for Micro-CT test. The porosity values of HD1-17 and SBT-R10 are close to the average porosity of all the marine shale samples. The porosity of sample LMS-T9 is also close to the average porosity of all the lacustrine shale samples (Table 1).

Table 1. The organic geochemistry, mineralogical composition and reservoir physical properties of the marine and lacustrine shale in the study area.

Shale Type	Sample NO.	Formation	Depth (m)/ Area	TOC (%)	R_b (%)	R_o (%)	Mineral Composition (%)					Brittleness Index	Porosity (%)	Permeability (md)
							Quartz	Feldspar	Carbonates	Pyrite	Clay			
	HD1-1	O_3w	1337.12	0.95	2.62	2.02	38.9	6.3	15.4	0.7	38.7	61.3	-	-
	HD1-2	O_3w	1336.26	2.7	2.68	2.06	35.4	5	16.1	6.8	36.7	63.3	7.16	0.328
	HD1-3	O_3w	1335.30	3.28	2.63	2.02	41.1	8.3	14.2	8.3	28.1	71.9	-	-
	HD1-4	O_3w	1334.26	2.99	2.58	1.99	40	4	20.4	4.1	31.5	68.5	3.27	0.027
	HD1-5	O_3w	1333.50	3.76	2.57	1.99	53.6	5	4.3	3.5	33.6	66.4	-	-
	HD1-6	O_3w	1333.20	3.98	2.72	2.08	89.6	0	5.6	4.8	0	100	-	-
	HD1-7	O_3g	1331.81	4.31	2.57	1.99	85	1.4	0	2.8	10.8	89.2	2.1	0.049
	HD1-9	S_1l	1329.66	3.2	2.58	1.99	53.1	11.3	6.1	3.7	25.8	74.2	2.5	0.001
	HD1-10	S_1l	1328.79	4.3	2.47	1.93	47	13.1	8.1	6.7	25.1	74.9	1.88	0.001
	HD1-11	S_1l	1327.74	4.43	2.52	1.96	39.5	13	12.8	6.4	28.3	71.7	-	-
	HD1-12	S_1l	1326.63	3.69	-	-	39.7	11.6	13.6	4.1	31	69	-	-
	HD1-13	S_1l	1325.65	4.23	-	-	36.6	10.2	24.5	2.2	26.5	73.5	1.9	0.001
	HD1-14	S_1l	1324.69	3.62	-	-	42.8	12.8	8.1	4	32.3	67.7	-	-
	HD1-15	S_1l	1323.82	3.39	-	-	3.5	0.8	0.3	49.4	46	54	1.83	0.224
	HD1-16	S_1l	1322.78	3.03	2.22	1.77	43.5	17	10.9	3.3	25.3	74.7	-	-
	HD1-17	S_1l	1321.80	3.54	-	-	33.7	11.9	25.6	3.3	25.5	74.5	3.26	0.017
	HD1-18	S_1l	1320.88	3.06	-	-	24.5	4.7	7.3	2.3	61.2	38.8	-	-
	HD1-19	S_1l	1320.07	3.28	2.53	1.96	37.3	7.2	7.8	3	44.7	55.3	3.86	0.005
	HD1-20	S_1l	1319.00	3.35	-	-	32.5	6.2	15.8	3.1	42.4	57.6	3.92	0.051
	HD1-21	S_1l	1317.77	3.47	-	-	40.1	6.7	11.5	2.7	39	61	1.99	0.007
Marine Shale	HD1-22	S_1l	1316.76	3.43	2.56	1.98	39	6.6	6.4	3.8	44.2	55.8	-	-
	HD1-23	S_1l	1315.82	3.82	-	-	45.3	6.4	10.2	4.7	33.4	66.6	2.39	0.007
	HD1-24	S_1l	1314.78	3.4	-	-	41.8	7.1	6.8	6	38.3	61.7	-	-
	HD1-25	S_1l	1313.91	3.7	-	-	43.4	5.4	8.3	2.5	40.4	59.6	2.45	0.006
	HD1-26	S_1l	1312.82	3.82	-	-	46.5	6.4	6	3.6	37.5	62.5	-	-
	HD1-27	S_1l	1311.84	3.44	2.12	1.71	43.4	6.3	5.5	2.2	42.6	57.4	-	-
	HD1-28	S_1l	1310.84	2.51	-	-	61.6	6.5	9.4	1.9	20.6	79.4	1.15	0.001
	HD1-29	S_1l	1309.91	2.81	-	-	59.3	6.4	3.6	2.3	28.4	71.6	-	-
	HD1-30	S_1l	1308.78	2.92	-	-	58.4	4.5	1.8	1.3	34	66	1.08	0.001
	SBT-R1	O_3w	SBT	3.44	2.04	1.66	48.7	1.1	0	1.1	49.1	50.9	5.19	0.861
	SBT-R2	O_3w	SBT	2.60	-	-	4.2	0	0	8.1	87.7	12.3	4.12	7.182
	SBT-R3	O_3w	SBT	3.40	1.64	1.41	87.7	0	0	0	12.3	87.7	-	-
	SBT-R4	O_3w	SBT	4.31	-	-	87.6	0	0	0	12.4	87.6	2.62	0.005
	SBT-R5	O_3w	SBT	4.28	1.19	1.14	100	0	0	0	0	100	3.30	0.010
	SBT-R6	O_3w	SBT	5.31	1.61	1.4	83	0	0	0	17	83	-	-
	SBT-R7	O_3g	SBT	6.00	-	-	54	8.4	0	1.1	36.5	63.5	-	-
	SBT-R8	S_1l	SBT	2.37	-	-	83.7	0	0	0	16.3	83.7	4.77	0.002
	SBT-R9	S_1l	SBT	1.83	2.41	1.89	72.4	8.3	0	0	19.3	80.7	2.46	0.002
	SBT-R10	S_1l	SBT	0.97	-	-	45	8.1	0	1.5	45.4	54.6	3.39	0.915
	SBT-R11	S_1l	SBT	1.94	-	-	41.3	3.8	0	4.2	50.7	49.3	4.16	0.532

Table 1. *Cont.*

Shale Type	Sample NO.	Formation	Depth (m)/ Area	TOC (%)	R_b (%)	R_o (%)	Mineral Composition (%)					Brittleness Index	Porosity (%)	Permeability (md)
							Quartz	Feldspar	Carbonates	Pyrite	Clay			
	SBT-R12	S_1l	SBT	1.78	-	-	41.7	6.4	0	0.6	51.3	48.7	4.72	0.680
	SBT-R13	S_1l	SBT	1.39	-	-	42.7	7.6	0	3.7	46	54	2.23	0.007
Lacustrine Shale	LMS-T1	$J_{1-2}z$ [1]	LMS	1.86	-	0.82	25	5	13	0	57	43	2.90	0.003
	LMS-T2	$J_{1-2}z$ [1]	LMS	1.09	-	0.64	42	7	0	0	51	49	3.60	0.380
	LMS-T3	$J_{1-2}z$ [1]	LMS	1.02	-	0.59	37	4	4	0	55	45	6.35	0.045
	LMS-T4	$J_{1-2}z$ [1]	LMS	1.72	-	0.63	46	8	0	0	46	54	2.84	0.500
	LMS-T5	$J_{1-2}z$ [1]	LMS	1.88	-	0.51	28	6	0	0	66	34	3.87	0.167
	LMS-T6	$J_{1-2}z$ [1]	LMS	1.41	-	0.57	18	5	2	0	75	25	3.83	0.063
	LMS-T7	$J_{1-2}z$ [1]	LMS	1.53	-	0.84	17	3	34	0	46	54	3.00	1.221
	LMS-T8	$J_{1-2}z$ [1]	LMS	3.61	-	0.73	17	4	8	3	68	32	6.94	0.396
	LMS-T9	$J_{1-2}z$ [1]	LMS	1.4	-	0.82	16	5	8	0	71	29	4.76	1.127
	LMS-T10	$J_{1-2}z$ [1]	LMS	1.13	-	0.67	11	0	49	1	39	61	6.63	1.230
	FY-10	$J_{1-2}z$ [1]	2810.12	1.74	-	1.23–2.09	16–35	4.3–5.2	0–23.8	0–5.1	46–68	40	4.5 (1.64–6.68)	0.134 (0.044–0.376)
	XL101	$J_{1-2}z$ [1]	2268.95	1.26	-	1.42	25.6	4.7	9.5	4.5	55.7	44.3	2.86	0.664
	HF-1	$J_{1-2}z$ [1]	2710.02	3.74	-	-	27.4	4.1	3.6	4	60.9	39.1	4.6	0.7269

[1] Where R_b is bitumen reflectance test results for marine shale, Ro is the test results of vitrinite reflectance for lacustrine shale and the calculated results of marine shale by the empirical formula *eq* $R_o = 0.618 R_b + 0.4$ [28]. The data of FY-10 are from [11]. The data of XL101 and HF-1 are from [10,29].

Table 2. The N_2 adsorption test results.

Shale Type	Sample NO.	Formation	Specific Area (m²/g)	Total Pore Volume (cc/g)	Mean Pore Diameter (nm)	Shale Type	Sample NO.	Formation	Specific Area (m²/g)	Total Pore Volume (cc/g)	Mean Pore Diameter (nm)
	HD1-M1	S_1l	35.95	0.05953	6.623		HD1-M22	S_1l	13.43	0.01615	4.811
	HD1-M2	S_1l	3.991	0.007563	7.58		HD1-M23	S_1l	11.57	0.01235	4.271
	HD1-M3	S_1l	21.41	0.08668	16.19		HD1-M24	S_1l	17.23	0.02027	4.707
	HD1-M4	S_1l	18.51	0.02768	5.981		HD1-M25	S_1l	17.73	0.02192	4.945
	HD1-M5	S_1l	35.74	0.05325	5.96	Marine shale	HD1-M26	S_1l	21.3	0.02111	3.965
	HD1-M6	S_1l	18.51	0.02768	5.981		HD1-M27	S_1l	34.35	0.04355	5.071
	HD1-M7	S_1l	4.728	0.007848	6.639		HD1-M28	S_1l	23.1	0.02637	4.565
	HD1-M8	S_1l	24.58	0.04076	6.634		HD1-M29	S_1l	16.8	0.02148	5.115
	HD1-M9	S_1l	26.92	0.06761	10.04		HD1-M30	S_1l	10.18	0.01313	5.157
Marine shale	HD1-M10	S_1l	17.67	0.03358	7.602		LMS-M1	$J_{1-2}z^1$	18.7	0.04417	9.447
	HD1-M11	S_1l	5.798	0.04927	33.99		LMS-M2	$J_{1-2}z^1$	22.75	0.05354	9.415
	HD1-M12	S_1l	11.6	0.02949	10.17		LMS-M3	$J_{1-2}z^1$	22.26	0.07386	13.27
	HD1-M13	S_1l	12.74	0.01587	4.98		LMS-M4	$J_{1-2}z^1$	19.02	0.04755	10
	HD1-M14	S_1l	3.455	0.0107	12.39	Lacustrine Shale	LMS-M5	$J_{1-2}z^1$	14.78	0.04274	11.57
	HD1-M15	S_1l	1.678	0.004379	10.44		LMS-M6	$J_{1-2}z^1$	13.22	0.03711	11.23
	HD1-M16	S_1l	4.511	0.01172	10.39		LMS-M7	$J_{1-2}z^1$	23.18	0.06262	10.81
	HD1-M17	S_1l	18.4	0.01831	3.98		LMS-M8	$J_{1-2}z^1$	8.889	0.02454	11.04
	HD1-M18	S_1l	15.82	0.01905	4.817		LMS-M9	$J_{1-2}z^1$	8.736	0.02563	11.73
	HD1-M19	S_1l	18.23	0.01706	3.744		LMS-M10	$J_{1-2}z^1$	13.31	0.0245	7.365
	HD1-M20	S_1l	19.32	0.01962	4.063		LMS-M11	$J_{1-2}z^1$	8.422	0.02367	11.24
	HD1-M21	S_1l	17.49	0.01861	4.257						

3.2. Analytical Methods

The total organic carbon (TOC) was tested at Key Laboratory of Shale Gas Exploration, Ministry of Land and Resources in China, Chongqing Municipality, China according to the Chinese National Standard methods GB/T 19145-2003 [30]. The shale samples were powdered to less than 200 mesh particles. Appropriate amount of the powder was weighed by removing the inorganic carbon with excess hydrochloric acid. Then, they were diluted to neutral with distilled water. Finally, they were dried to determination, with 17 °C and 59% RH humidity [4]. The TOC can be expressed as the weight percent, which is calculated by the formula:

$$TOC = (W_R/W_T) \times 100 \qquad (1)$$

where TOC is the total organic carbon, %; W_R and W_T are the residual weight after dried and the total weight of the powder, respectively, g.

The thermal evolution of the organic matter was tested in the Engineering Research Center for Shale Gas Resource and Exploration, Chongqing Institute of Geology and Mineral Resources, China. The thermal evolution of the lacustrine shale was determined by the vitrinite reflectance (R_o). Vitrinite reflectance was measured by a Leitz MPV-3 micro-photometer under the oil immersion reflected optical light according to the Chinese National Standards GB/T 6948-1998 [31]. For each sample, about 30 different vitrinite observation points were randomly selected for measurements and the averaged data were used. The thermal evolution of marine shale was determined by the bitumen reflectance (R_b). The bitumen reflectance was measured with a polarizing microscope Germany Lycra Axioscope A1 and American CRAIC spectrophotometer +MSP 400. All tests were conducted in accordance with Chinese Industrial Standard SY/T 5124-2012 [5].

X-ray diffraction (XRD) was tested at Key Laboratory of Shale Gas Exploration, Ministry of Land and Resources in China, Chongqing Municipality, China. The shale samples were powdered less than 200 mesh (i.e., <75 lm). Then, the powder was tested with a Bruker D8 DISCOER diffractometer (Co Kα-radiation, 45 kV, 35 mA) according to the two independent processes of the CPSC procedure. The diffracted beam was tested with scintillation at 0.02° 2 θ step size and 20 s step time. Diffractograms are derived from 2° to 76° 2 θ [32].

The field emission scanning electron microscopy (FE-SEM) was tested in Engineering Research Center for Shale Gas Resource and Exploration, Chongqing Institute of Geology and Mineral Resources, China. The shale samples were polished with argon ion milling instrument (Hitachi High-Tech IM4000). After the argon-ion-beam milling, the vertical sectioned samples were coated with carbon. The samples were inserted into an FEI Helios NanoLabTM 650 DualBeam FIB-SEMTM for imaging and SEM Maps [1]. Images were taken using back-scattered electron at 5 kV acceleration voltage and a working distance of 4 mm [33].

Nitrogen adsorption was tested by the Micromeritics ASAP 2420 instrument. The samples were pulverized to about 60–80 mesh. About 1.5–2.5 g pulverized samples was used for nitrogen adsorption tests. Then, degassing was performed at an ambient temperature of 25.0 °C before testing N adsorption and desorption amounts. After degassing, the N2 adsorption amount was tested at −195.8 °C, with an increase in the P/P$_o$ from 0.01 to 0.99. Then, keep the equilibration about 10 s. During the desorption process, P/P$_o$ was decreased from 0.99 to 0.14. The N_2 desorption isotherms were approximately obtained [34].

Helium porosity was tested at Sichuan Kelite Oil and Gas Technology Service Company Limited (Chengdu, China), China. The samples were drilled to a diameter of 2.54 cm and length of 5 cm for porosity and permeability tests. The porosity was calculated by dividing the pore volume from the total volume according to Chinese national standard GB/T 29172-2012 [1].

Pulse permeability was tested at Sichuan Kelite Oil and Gas Technology Service Company Limited (Chengdu, China), China with YCS-II briquette and a rock permeability tester at 17 °C temperature and 55–60% humidity [5]. The permeability was measured

by pressure pulse attenuation method, which is a non-steady permeability test method, according to the Chinese National Standard GB/T 34533-2017 [1,35].

The Micro-CT scans were tested by a compact laboratory CT system (GE phoenix nanotom m 180). First, core plugs were drilled with 50 mm length. Then, the samples were scanned over 360° by a large field of view mode, with an exposure time of 120 s, and 1600 slices were collected from this scanning process [1]. Finally, the 3D image of the sample was generated from Avizo Fire 8.1 by importing data into it. The quantitative analyses of the pore length and width were conducted on the rendered volumes in Avizo by assigning different gray scale values to the microstructural features of interest. The pore throat connectivity was qualitatively determined based on the gray scale values of different segmentations [36].

4. Results

4.1. Organic Geochemical Characteristics

4.1.1. Total Organic Carbon Contents

As shown in Table 1, the TOC of marine shale samples ranges from 0.95% to 4.43%, with an average of 3.39% in well HD-1 at about 1330 m depth (Figure 2), which is similar to the TOC of the marine shale at SBT outcrops in the range of 0.97% to 6.00% (average 3.05%). The TOC of the lacustrine shale ranges from 1.02% to 3.61%, with an average of 1.66% at the LMS outcrops, which is similar to the TOC of the Dongyuemiao shale drilled at the depth of 2268–2810 m as well. In well FY-10, the range is from 0.16% to 4.04%, with an average of 1.74% [11], and the average of TOC is 1.26% and 3.74% in wells XL101 and HF-1, respectively [29].
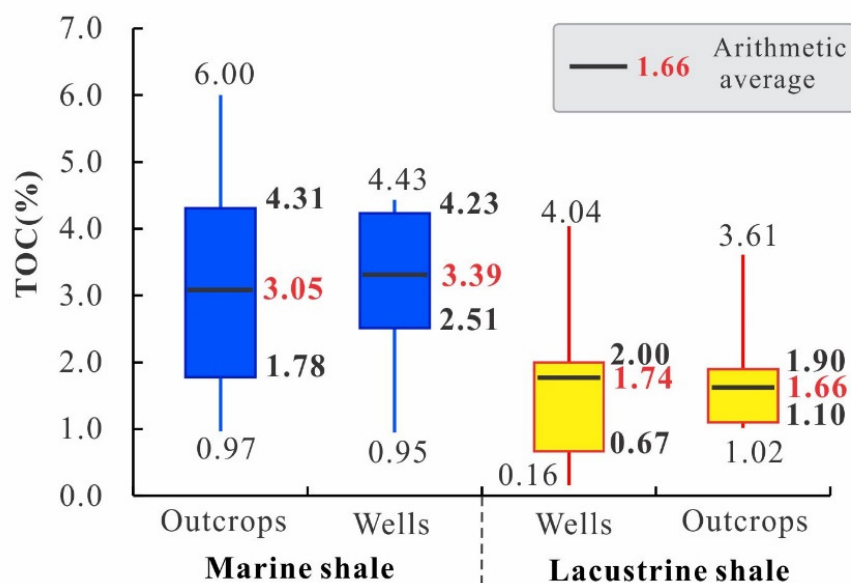
Figure 2. The TOC content of the marine and lacustrine shale samples from the wells and outcrops.

4.1.2. Maturity of Organic Matter

Considering that there is no vitrinite in the marine shale kerogen, the maturity of the marine shale was tested by bitumen reflectance (R_b). Then, the equivalent vitrinite reflectance (eq R_o) was calculated by the empirical formula eq $R_o = 0.618 R_b + 0.4$ [28]. As shown in Table 1, the eq R_o of marine shale samples ranges from 1.71% to 2.08%, with an average of 1.96% in well HD-1 at about 1300 m depth, which is larger than the eq R_o of samples from SBT outcrops that range from 1.14% to 1.89%, with an average 1.50%. The R_o of lacustrine shale ranges from 1.23% to 2.09% (av. 1.64%) sampled from the wells at a depth of 2268–2810 m, which is much more mature than the R_o of samples from LMS outcrops, which are in the range of 0.51% to 0.84% (average 0.68%).

4.2. Mineralogy

The mineral component of marine and lacustrine shale samples is presented in Table 1 and Figure 3. It shows that all the shale samples are mainly composed of quartz, feldspar, carbonates, pyrite and clay. The quartz content in the marine shale is much richer than that in the lacustrine shale. In the marine shale, the quartz contents range from 3.5% to 100%, with an average of 49.7%. Most of them are larger than 35%. The quartz content is smaller than 10% in the bentonite which is a millimeter-scale interlayer in marine shale, such as in samples HD1-15 and SBT-R2 in Table 1. Most of the quartz content in marine shale is larger than 35%. Especially, the quartz content is 100%, as observed in the siliceous shale in the Wufeng Formation (Table 1). The quartz contents range from 11% to 46%, with an average of 25.8% in the lacustrine shale samples, which is obviously smaller than in the marine shale. Both the marine and lacustrine shale also contain abundant clay minerals. In the marine shale, the clay mineral content ranges from 0 to 87.7%, with an average 33.23%, which is smaller than in the lacustrine shale (39–75%, average 57.4%).
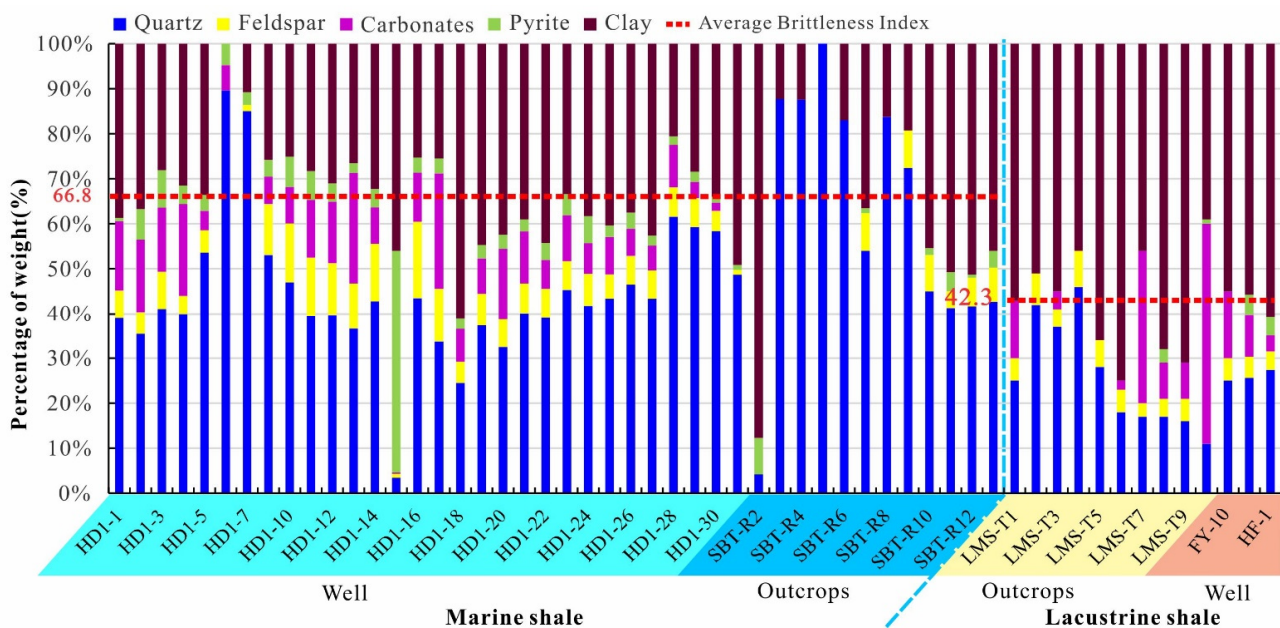
Figure 3. The mineral characteristics of the marine and lacustrine shale samples.

It is generally accepted that, the richer the content of brittle minerals, the more favorable they are for later reservoir reconstruction. The brittleness index has been used to characterize the brittleness of shale, and brittle minerals mainly include carbonate, quartz, feldspar and pyrite [37]. According to the brittleness index calculation formula [38]:

$$BI = (W_Q + W_F + W_C + W_D)/W_T \qquad (2)$$

where BI is the brittleness index, W_Q, W_F, W_C and W_D are the weights of quartz, feldspar, calcite and dolomite, respectively, and W_T is the total mineral weight.

The brittleness index of all the shale samples was calculated (Table 1). The results show that the distribution span of the brittleness index of marine shale is large (12.3–100), and the average value is 66.8. The brittleness index of lacustrine shale ranges from 25 to 61, with an average value of 42.3 (Figure 3).

4.3. Pore Morphology Analyses Based on FE-SEM Images

An FE-SEM image is mainly used to qualitatively characterize the pore structure characteristics of shale, such as the distributions, shapes, sizes and arrangement of pores [39]. The FE-SEM images show that many micro-nano pores are in marine and lacustrine shale samples. According to the relationship between pores and minerals, the pores can be

mainly divided into the following three categories: organic-matter-hosted pores (OM pores), dissolution pores and intergranular pores.

The OM pores are mainly in the organic matter (Figure 4a–d). Previous studies recognized that the formation of OM pores is mainly controlled by kerogen type, organic matter abundance and thermal evolution degree [40,41]. In the Eastern Sichuan Basin, many OM pores are developed in both marine and lacustrine shale samples. The OM pores possess strong microscopic heterogeneity, and their pore diameters vary between several nanometers and hundreds of nanometers. The OM pores in the lacustrine shale (Figure 4b) are obviously more circuitous and jagged than in the marine shale (Figure 4c). The diameter of the OM pores in lacustrine shale is smaller than in marine shale. In the lacustrine shale, all the OM pores are arranged in a disorderly manner in the organic matter (Figure 4b,d). In the marine shale, most of the OM pores are arranged in a disorderly manner in the organic matter (Figure 4a) as well. However, part of the OM pores involves directional alignment in postmature organic matter, which is obviously influenced by extrusion stress (Figure 4c). Previous studies concluded that OM pores are mainly formed during the kerogen thermal cracking stage [41]. The diameter of OM pores likely increases as kerogen thermally cracks, which may lead to the strength of the organic matter decreasing. Hence, the OM pores are more likely to be affected by burial compaction or tectonic stress.

In this work, the dissolution pores are mainly observed in the organic matter (Figure 4c,d) and the clearance between the minerals (Figure 4e,f). The shape of the pores is mainly round or approximately round. The wall of holes is smooth, which indicates that the pores are likely connected with other pores as a migration method for the fluid, such as water or hydrocarbon fluid. The diameter of these pores is mainly wider than 2 μm, which is obviously larger than the OM pores. However, the dissolution pores in the lacustrine shale are much wider than those in the marine shale. The diameter of the dissolution pores in lacustrine shale is commonly larger than 50 μm, which is likely correlated to the discharge of the formation water in the burial process. Meanwhile, the dissolution pores in the lacustrine shale are commonly isolated from each other (Figure 4f). The dissolution pores in the marine shale are partly connected with each other, which may indicate that the fluid is not discharged from the shale easily after the diagenesis of shale. The dissolution pores are connected with each other by the micro-fractures in the overpressure unit (Figure 4e).
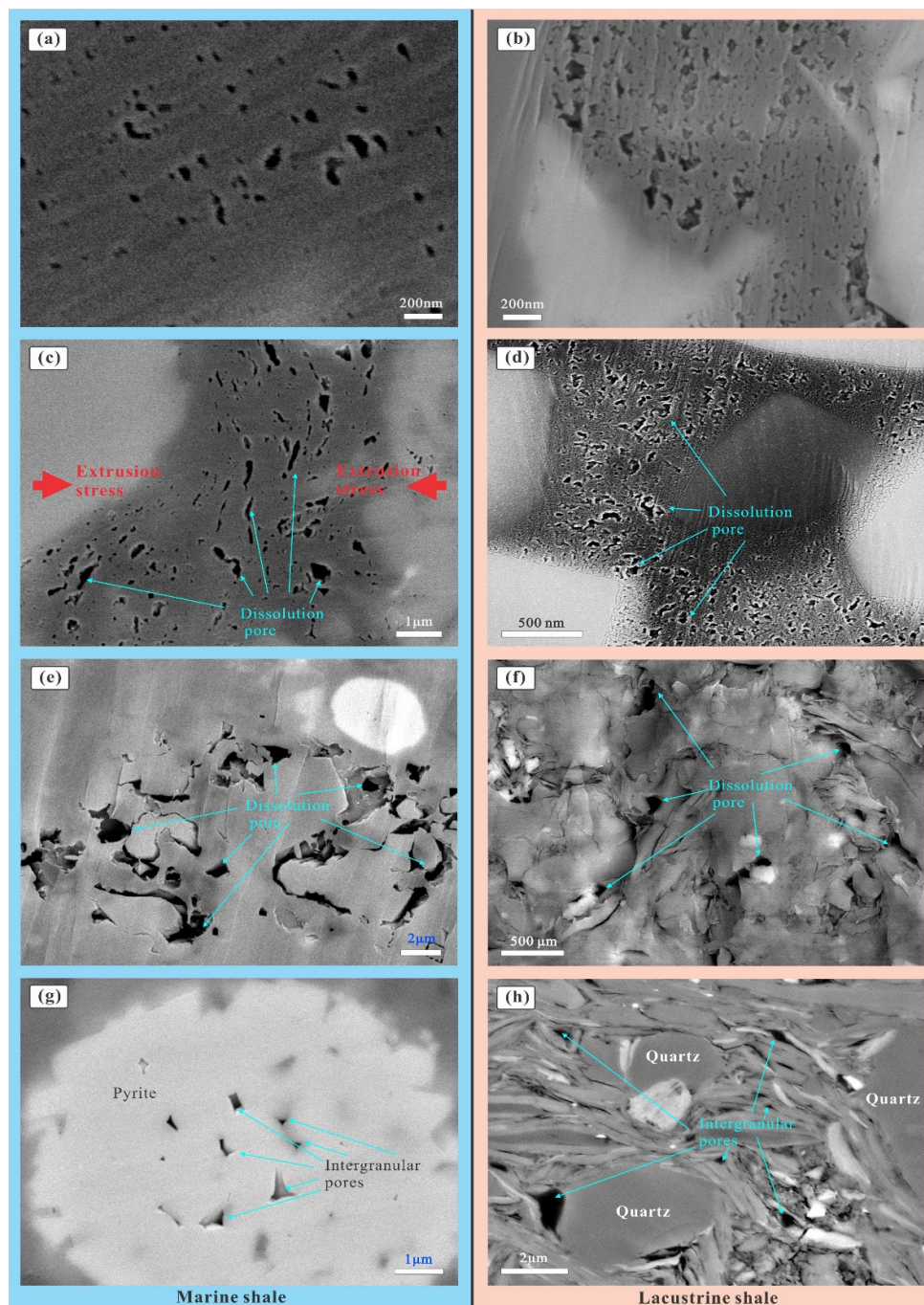
The intergranular pores are also observed in the marine and lacustrine shale (Figure 4g,h). In the marine shale, the intergranular pores are mainly observed between the particles of pyrite. They are mainly an angular shape, with a diameter smaller than 1 μm. In the lacustrine shale, the intergranular pores are not only observed in the crystal druse of pyrite but also between the clay mineral and quartz (Figure 4h). The diameter of the intergranular pores ranges from several nanometers to several micrometers, with various shapes. The diameter and the shape of the intergranular pores are dominated by the arrangement of the minerals and the diameter of the minerals. As the diagenesis progressed, the intergranular pores gradually reduced for the mineral crystallization, tending to parallel arrangement and the cementation of the strata fluid. Hence, the intergranular pores are much fewer than in the lacustrine shale.

4.4. Microscopic Pore Structure Characteristics

It is known that the gas in shale is mainly in the adsorption and free state [42]. The gas in shale is mainly adsorbed in the mesopores (the diameter is 2–50 nm) and micropores (diameter < 2 nm). The free gas is mainly trapped in the macropores (diameter > 50 nm) [29]. The N_2 adsorption can well characterize the content of the mesopores and micropores. Hence, N_2 adsorption is commonly used to study the mesopores and micropores of shale.
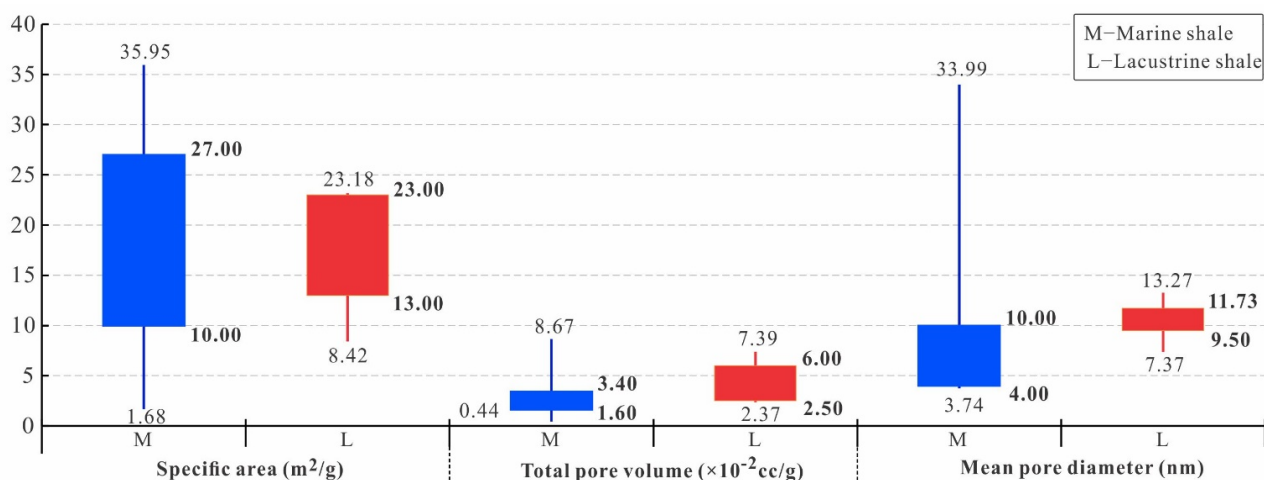
As shown in Figure 5 and Table 2, the specific area of marine shale ranges from 1.68 to 35.95 m^2/g, with an average of 16.75 m^2/g. In the lacustrine shale, the specific area ranges from 8.42 to 23.18 m^2/g, with an average of 15.75 m^2/g, which is smaller than the marine shale. The total volume of the pores ranges from 0.0044 to 0.0867 cc/g, with an average of 0.027 cc/g in the marine shale, which is smaller than that in the lacustrine shale. In the

lacustrine shale, the total volume of the pores ranges from 0.0237 to 0.0739 cc/g, with an average of 0.0418 cc/g. The mean pore diameter of the marine shale ranges from 3.74 nm to 33.99 nm, with an average of 7.5 nm, which is narrower than that in the lacustrine shale (7.37–13.27 nm, av. 10.647 nm).


Figure 4. The pore morphological characteristics in the FE-SEM images. (**a**) The OM pores in the marine shale. (**b**) The OM pores in the lacustrine shale. (**c**) The dissolution pores in the organic matter are deformed by the extrusion stress in the marine shale. (**d**) Part of the OM pores were dissolved in the lacustrine shale. (**e**) The dissolution pores in the marine shale are partly connected with each other by the micro-fractures. (**f**) The dissolution pores in the lacustrine shale are isolated from each other. (**g**) In marine shale, the intergranular pores in the clusters of pyrite crystals. (**h**) The lacustrine shale; the intergranular pores are commonly observed between the mineral particles.

Figure 5. The specific area, total pore volume and mean pore diameter from the N_2 adsorption test results.

The adsorption isotherms of each shale sample are different, which is mainly caused by the strong heterogeneity of shale [43]. As shown in Figure 6, the N_2 adsorption amount gradually increases with increasing pressure, and the phenomenon of saturated adsorption is not shown until the relative pressure is close to 1.0, reflecting the presence of macropores in both marine and lacustrine shales [44]. Although the adsorption isotherms of each sample are slightly different in morphology, they all exhibit anti-S type with increasing relative pressure. This means that the adsorption isotherms of shales belong to typical IV-type isotherms, indicating that the pores in the shales are a complete pore system range continuously from micropores to macropores. In all the shale samples, the adsorption and desorption curves overlap at a relatively low pressure (0–0.4); thus, no adsorption loop would form, while a large adsorption loop would form at a relatively high pressure (0.4–1.0). When the pressure is approaching 0.5, there is a turning point at which a sharp drop could occur in the desorption curve. It is indicated that the samples are of small-caliber and large-volume pores, where microcracks are better developed. These kinds of pores are beneficial for adsorption of gas but are not conductive to desorption and diffusion due to their bad ventilation [45]. Although the total pore volume of sample HD1-M10 is smaller than that of sample LMS-M5, the desorption curve of sample HD1-M10 drops much more sharply than the desorption curve of sample LMS-M5, which indicates that marine shale is more obviously characterized by small-caliber and large-volume pores.
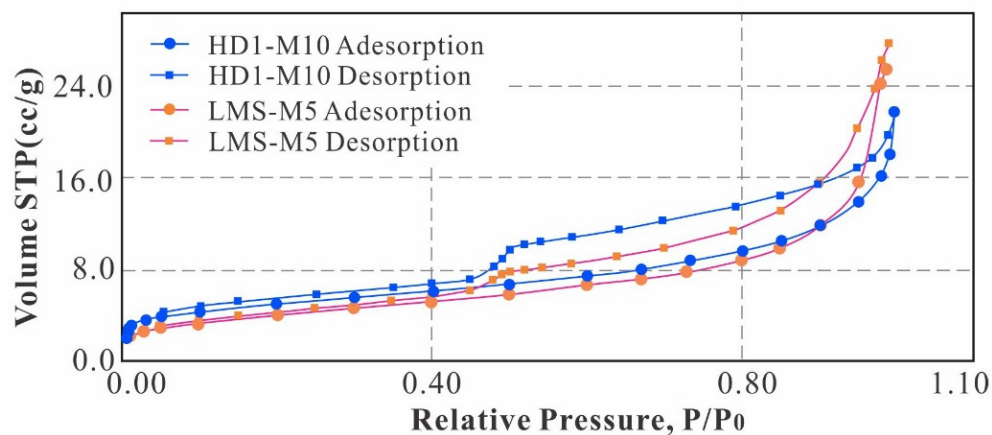

Figure 6. The adsorption and desorption curves of the typical marine and lacustrine shale samples based on the N_2 adsorption tests.

4.5. Reservoir Physical Property

The porosity of marine shale samples varies from 1.08% to 7.16%, with an average of 2.76% in well HD-1, which is a little smaller than in the SBT outcrops. The porosity of the sample ranges from 2.23% to 5.19%, with an average of 3.69%. The porosity of the lacustrine shale is larger than that of the marine shale. The porosity of the lacustrine shale varies from 2.84% to 6.94%, with an average of 4.47% in the outcrops LMS and in the range 1.64–6.68%, with an average of 4.5% in the wells (Table 1).

An extreme variation is observed in the test results of shale permeability. In the SBT outcrops, the permeability of the marine shale varies from 0.002 to 7.18 md, with an average 0.872 md, which is much larger compared to the core samples from well HD-1. The permeability of the marine shale from well HD-1 ranges from 0.001 to 0.328 md, with an average 0.052 md (Table 1). In the lacustrine shale, the permeability in the outcrops is larger than from the wells as well. In the outcrops LMS, the permeability of the shale varies from 0.003 to 1.23 md, with an average 0.513 md, which is larger compared to the core samples (0.44–0.729 md, av. 0.134 md). As shown in Figure 7, the reservoir physical property of the lacustrine shale is better than marine both in porosity and permeability.
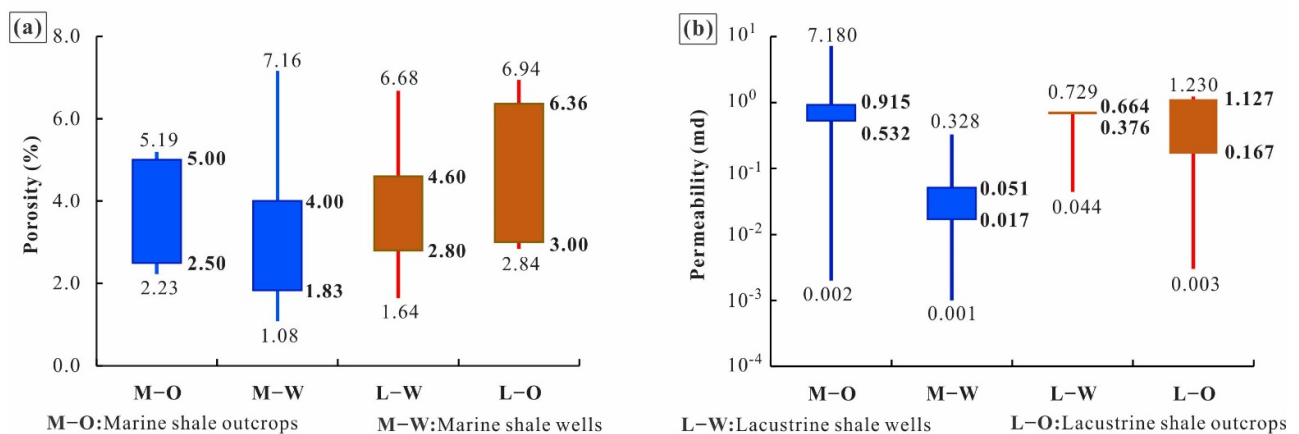
Figure 7. The reservoir physical properties of the marine and lacustrine shale samples. (**a**) The porosity tested results of the marine and lacustrine shale; (**b**) The permeability tested results of the marine and lacustrine shale.

5. Discussion

5.1. Difference in Formation Mechanism of the Pores

Shale is defined as a type of tight rock. During the burial process, a large number of the pores in it are compacted by the compaction of overlapped strata. As mentioned above, the resident pores in the shale are mainly of three types: OM pores, dissolution pores and intergranular pores.

The OM pores are commonly in nanometer-scale, with the protection of an organic matter framework, which is a benefit in terms of not being destroyed by the compaction. Meanwhile, the kerogens are cracked to oil and gas with thermal evolution, which not only contributes to the formation of OM pores but also the formation of overpressure in the shale, which can offset part of the compaction in shale. Hence, it is generally acknowledged that a higher TOC content means a stronger shale gas storage capacity [46]. However, with kerogen cracking progression, the diameter of the OM pores becomes more and more wide. The OM pores may be compacted by extrusion stress (Figure 4c). Hence, the porosity of over-mature shale may increase first and then decrease slightly or even present a negative correlation directly with the increase in TOC content [41]. Compared to lacustrine shale, marine shale is much more organic-rich (Figure 2). Meanwhile, there is a positive correlation between content of TOC and quartz and clay mineral in marine shale (Figure 8), which indicates that the endogenous inputs and the adsorption of the clay mineral contribute to the enrichment of organic matter in marine shale [47]. It is obviously different from

lacustrine shale, in which the organic matter is coming from both the terrestrial organic matter and algae in the paleo-lake [18]. There is no obvious correlation between content of TOC and quartz and clay mineral in lacustrine shale (Figure 8). Meanwhile, there is a positive correlation between TOC content and porosity in marine shale (Figure 9), which is consistent with the character of the pore structures based on the N_2 adsorption results (Figure 6). However, there is no obvious correlation between TOC content and porosity in lacustrine shale (Figure 9). This may be caused by the small contribution of OM pores to the porosity in lacustrine shale regarding the low TOC content (Figure 2) and low thermal evolution stage (Table 1) of the lacustrine shale.
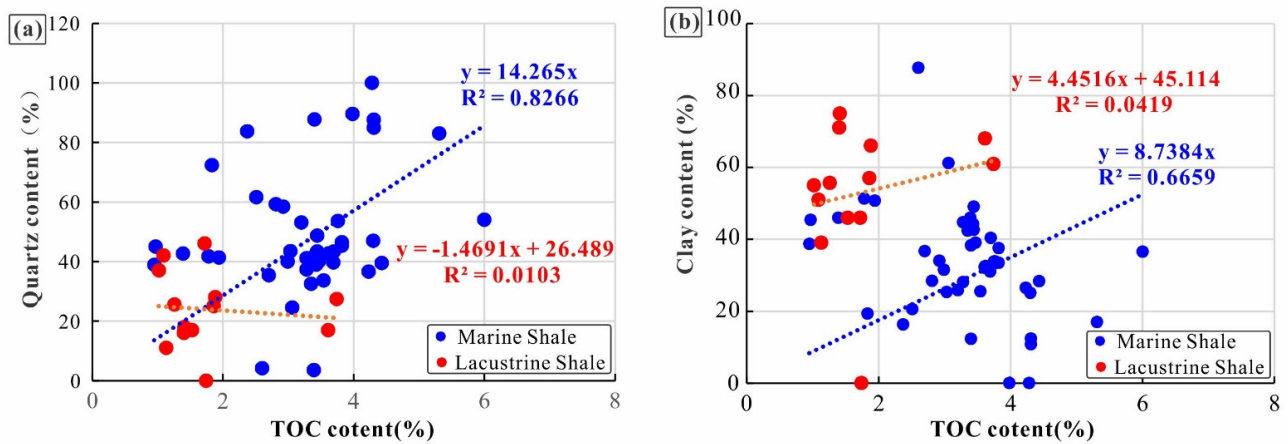
Figure 8. The correlation between TOC and mineral content. (**a**) The correlation between TOC and quartz content. (**b**) The correlation between TOC and clay content.
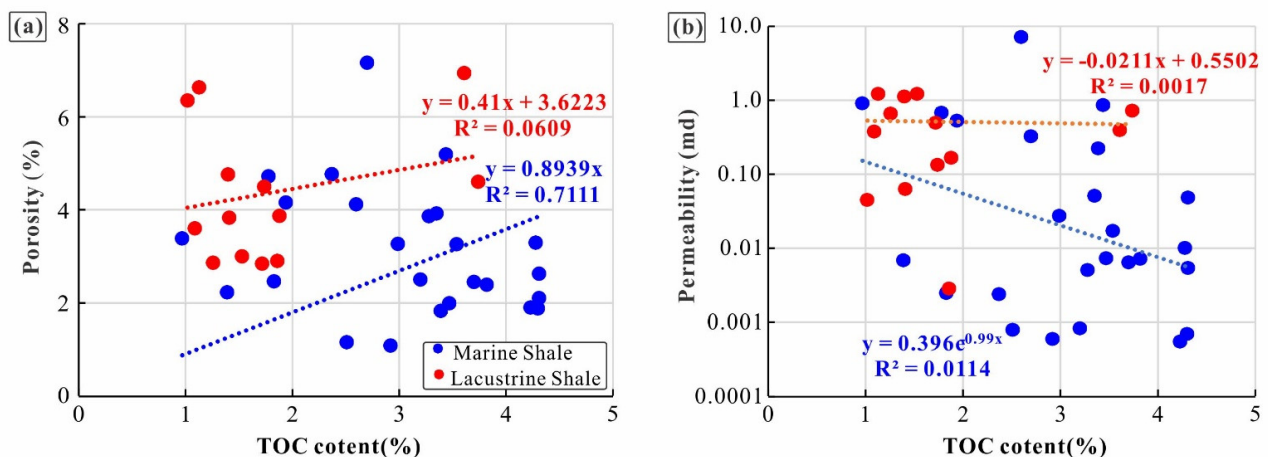

Figure 9. The correlation between TOC and reservoir physical property. (**a**) The correlation between TOC and porosity. (**b**) The correlation between TOC and permeability.

In the early diagenesis stage, the water in sediment is expelled through a large number of isolate pores by compaction. With the fluid flowing out, a few macropores are formed in sediments (Figure 4f) by the fluid pressure and the dissolution of part of the pore wall. In the middle diagenesis stage, framework minerals undergo corrosion for generation of organic acids, forming intraparticle dissolution pores. However, part of the pores may be cemented with the diagenesis. The fluid in the strata cannot be expelled and is entrapped in the local area. As the fluid becomes entrapped more and more, the overpressure is formed. The pores are connected in some local area with the corrosion curves (Figure 4e). As shown in Figure 4e,f, the dissolution pores in lacustrine shale are mainly formed by the expulsion of fluid in the shale. The dissolution pores in marine shale are mainly formed by the corrosion of organic acids.

The intergranular pores are associated with the framework of mineral particles, especially best developed in pressure shadows of brittle particles, which can protect these pores from collapse. In addition, due to the strong plasticity of clay minerals [48], it is easy to be compacted and deformed; thus, rigid particles have a significant effect on the preservation of intergranular pores. As shown in Figure 3, the brittle index of marine shale is larger than in lacustrine shale. However, merely a few intergranular pores are observed in the marine shale (Figure 4g). The intergranular pores are commonly observed in the lacustrine shale samples. The contribution of the intergranular pores is obviously smaller in the marine shale than in the lacustrine shale.

5.2. Arrangement Differences of the Pores

As shown in Figure 9, the TOC is positively correlated to the porosity ($R = 0.84$), but there is no obvious correlation between TOC and permeability. Meanwhile, the porosity of the marine shale is smaller than that of the lacustrine shale (Figure 7), while the permeability is similar. This indicates that the permeability of the shale is not only influenced by the porosity but also by the arrangement of the pores. As shown in Figure 10, the distribution of the pores is obviously different in marine and lacustrine shale. In the marine shale (Figure 10a), a few pores are connected in the horizontal direction as cluster pores. The past channels are characterized by the linear parallelism pores, which had been the migration path for the fluid in the early to middle diagenesis stage. They are oblique in arrangement. Part of the past channel is blocked by the cemented or squeezed action during the diagenesis process. The pores in the past channel are mainly in the nanometer-scale and intermittently connected. The cluster pores are levitated in the shale as kites and connected by the past channels. In the cluster pores, the pores are connected with each other, with the overpressure to offset the vertical extrusion stress. It is consistent with the N_2 adsorption results as well (Figure 6), which are characterized by small-caliber and large-volume pores. In the lacustrine shale (Figure 10b), the cluster pores and the past channels are mainly arranged according to the flow channels in the vertical direction. Although there are more past channels in lacustrine shale than in marine shale, merely a few past channels are connected with the cluster pores. Hence, although the porosity of the lacustrine shale is larger than the marine shale, the permeability is similar to marine shale (Figure 7).
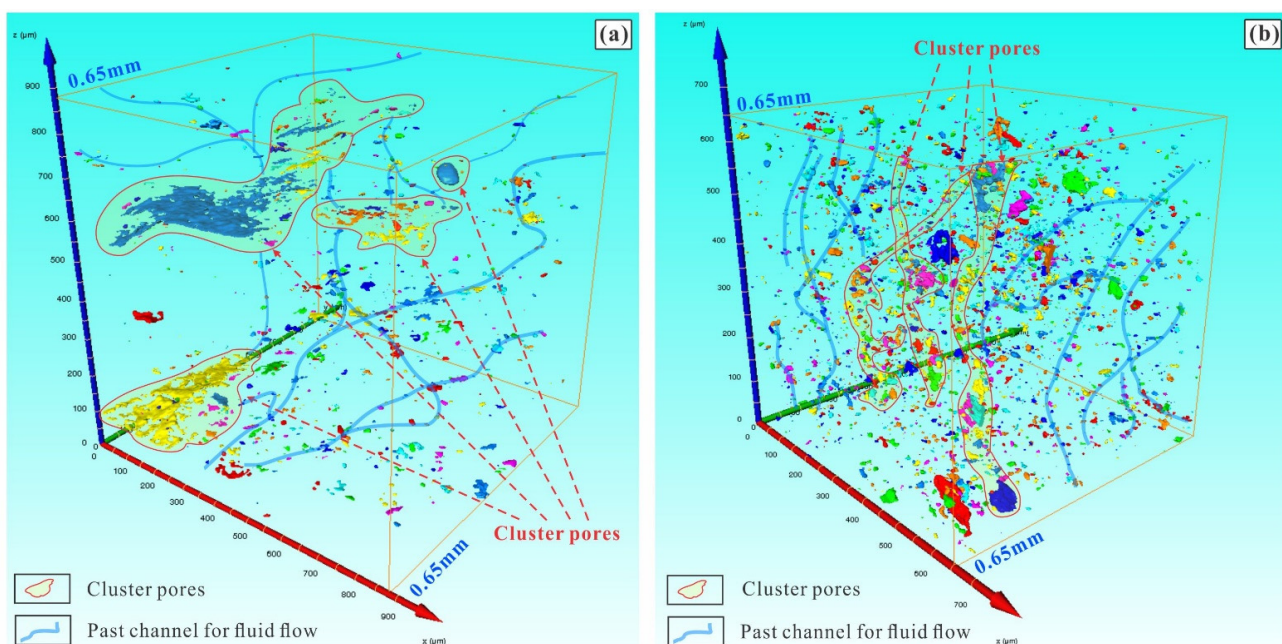
Figure 10. The arrangement characteristics of the pores in the Micro-CT images. (**a**) The pores distribution in marine shale sample HD1-17. (**b**) The pore distribution in lacustrine shale sample LMS-T9.

5.3. Difference in Tectonic Evolution

As mentioned above, the lacustrine shale is obviously different from the marine shale in the formation mechanism and arrangement of the pores, which is not only controlled by the material basis but also the thermal degradation and the compaction during their burial process. The equivalent vitrinite reflectance of the marine shale is 1.50% and 1.96% in the outcrops and well, which is more mature than the lacustrine shale, with R_o 0.68% and 1.64% in the outcrops and well, respectively (Table 1). The lacustrine shale has entered into the mature to wet gas stage [49]. According to the thermal model based on the test results of fluid inclusions [11], the lacustrine shale experienced the maximum formation temperature of about 140 °C, with a burial depth of about 4500 m (Figure 11a). The kerogen in lacustrine shale is mainly converted to oil and gas condensate in the Eastern Sichuan Basin. In this process from solid kerogen to oil gas mixture, the volume is not increasing as sharply as in the marine shale. Meanwhile, the TOC in lacustrine shale is smaller than that in marine shale. The hydrocarbon generation pressurization is not as obvious as in the marine shale either. Hence, the cluster pores are mainly in a vertical direction along the fluid flow channel. The marine shale experienced a maximum formation temperature of about 210 °C, with a burial depth of about 6000 m (Figure 11b). The marine shale progressed to the high to over-mature stage. It is indicated that residual liquid hydrocarbon and heavy hydrocarbon gas had been completely converted to gas before being uplifted [47]. Hydrocarbon generation pressurization is more easily formed, which is a benefit to the pores to offset compaction. The lateral permeability is commonly larger than the vertical permeability of marine shale [50]. Its TOC is richer than that of lacustrine shale. The OM pores are more easily connected with each other at the adjacent organic matter, with the action of hydrocarbon generation pressurization. Hence, the cluster pores in marine shale are approximately parallel to the bedding (Figure 10).
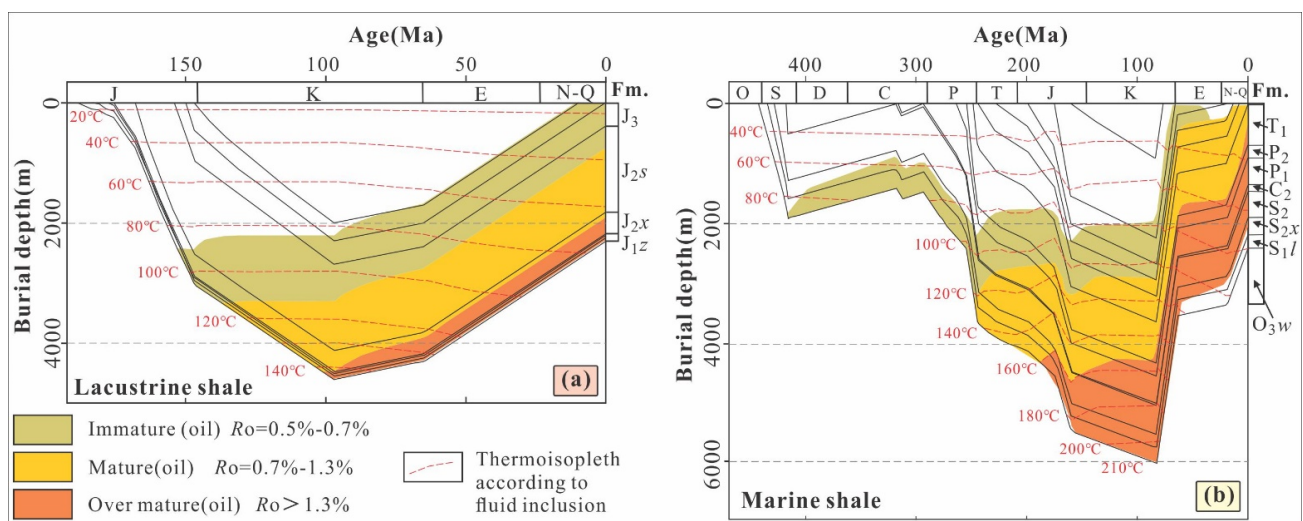
Figure 11. The tectonic evolution characteristics of the marine and lacustrine shale. (**a**) The burial and thermal history of the lacustrine shale in Ziliujing Formation in Fuling area, modified from [10]. (**b**) The burial and thermal history of the marine shale in Wufeng–Longmaxi Formation in well JY1 (Figure 1), modified from [47].

In the Eastern Sichuan Basin, the lacustrine shale (Dongyuemiao Member) is overlapped on the marine shale (Wufeng–Longmaxi Formation). The maximum burial depth of the marine shale experienced is larger than that of the lacustrine shale (Figure 11). According to the burial history model (Figure 11), the lithostatic pressure is about 117 MPa at the deepest burial stage of lacustrine shale, estimated with the average density 2.6 kg/m^3 for the upper formation. The lithostatic pressure is about 156 MPa at the deepest burial stage of marine shale, which is about 39 MPa larger than the lacustrine shale experienced.

Meanwhile, the marine shale that has undergone compaction action time is much longer than lacustrine shale (Figure 11). Hence, the past channels are mainly low-angle-inclined in the marine shale and high-angle-inclined in the lacustrine shale (Figure 10). It is indicated that the influence of compaction action on the pores is more obvious in the marine shale than in the lacustrine shale.

6. Conclusions

According to geochemical, mineral, imaging and physical tests in Wufeng–Longmaxi shale and Dongyuemiao shale, this work compared the differences in pore characteristics and influencing factors regarding the marine and lacustrine shale in the Eastern Sichuan Basin. Following are the main conclusions drawn from the study:

(1) The TOC of the marine shale is in the range of 0.97–6.00%, with an average 3.39%, which is richer than the lacustrine shale, with an average 1.74%. Meanwhile, the thermal evolution of the marine shale (av. *eq* R_o = 1.96%) is also more mature than the lacustrine shale (av. R_o is 1.64% in well and 0.68% in outcrops). These are benefits of OM pores formation in marine shale. In marine shale, TOC is positively correlated to porosity. Few intergranular pores are observed in the FE-SEM images. It is indicated that the pores in the marine shale are mainly composed of OM pores. However, there is little correlation between TOC content and porosity in the lacustrine shale. Dissolution pores and intergranular pores are commonly observed in the FE-SEM images. It is indicated that the pores in the lacustrine shale are mainly composed of dissolution pores and intergranular pores. This difference is not only correlated to the difference in TOC content but also the difference in thermal evolution. In the over-mature stage, the OM pores would be expanded, with the kerogen cracking and hydrocarbon generation pressurization.

(2) The arrangement of the pores is obviously different in marine and lacustrine shale. In the marine shale, the cluster pores are levitated in the shale as kites and connected by past channels. The marine shale is characterized by small-caliber and large-volume pores. However, in the lacustrine shale, the cluster pores and the past channels are mainly arranged according to the flow channels in the vertical direction. Although the porosity of the marine shale is smaller than that of the lacustrine shale, the permeability is similar in each. No obvious correlation has been observed between porosity and permeability in the shale. The permeability of the shale is likely dominated by the arrangement of the pores.

(3) The arrangement of the pores in marine shale is obviously deformed by compaction. Hydrocarbon generation pressurization is a benefit to the pores to offset the compaction, which promotes formation of lateral cluster pores. However, in lacustrine shale, although the porosity of the core samples is smaller than in the outcrops, the pores are not obviously compacted with the characteristic of lateral arrangement. The lacustrine shale is characterized by under-compaction, which commonly results from fluid pressure conducted upward by the vertical channels. The compaction action is stronger in marine shale than in lacustrine shale in the Eastern Sichuan Basin, China.

Hence, it can be deduced that the sweet spots for lacustrine shale gas are likely located at the areas characterized by under-compaction resulting from the fluid pressure conducted upward, such as the hinge zone of syncline or the core of anticline overlap on gas reservoirs.

Author Contributions: J.H.: experiment, data evaluation, conceptualization, methodology and writing of original draft manuscript. A.Z.: sampling and experiment. L.Z.: drawing and experiment. D.W.: sampling and field geological survey. Z.Q.: data evaluation and supervision. P.Y.: experiment and data evaluation. All authors have read and agreed to the published version of the manuscript.

Conflicts of Interest: The authors declare no conflict of interest.

References

1. He, J.; Wang, J.; Yu, Q.; Liu, W.; Ge, X.; Gou, Q.; Qiu, Z. The discovery of exogenous type shale gas and its application to the hydrocarbon exploration. *Acta Pet. Sin.* **2018**, *39*, 12–22.
2. Zhao, B.; Li, R.; Qin, X.; Wang, N.; Zhou, W.; Khaled, A.; Zhao, D.; Zhang, Y.; Wu, X.; Liu, Q. Geochemical characteristics and mechanism of organic matter accumulation of marine-continental transitional shale of the lower permian Shanxi Formation, southeastern Ordos Basin, north China. *J. Pet. Sci. Eng.* **2021**, *205*, 108815. [CrossRef]
3. Dai, J.; Zou, C.; Dong, D.; Ni, Y.; Wu, W.; Gong, D.; Wang, Y.; Huang, S.; Huang, J.; Fang, C.; et al. Geochemical characteristics of marine and terrestrial shale gas in China. *Mar. Pet. Geol.* **2016**, *76*, 444–463. [CrossRef]
4. Shi, X.; Wu, W.; Wu, Q.; Zhong, K.; Jiang, Z.; Miao, H. Controlling Factors and Forming Types of Deep Shale Gas Enrichment in Sichuan Basin, China. *Energies* **2022**, *15*, 7023. [CrossRef]
5. Shi, X.; Wu, W.; Shi, Y.; Jiang, Z.; Zeng, L.; Ma, S.; Shao, X.; Tang, X.; Zheng, M. Influence of Multi-Period Tectonic Movement and Faults on Shale Gas Enrichment in Luzhou Area of Sichuan Basin, China. *Energies* **2019**, *15*, 6846. [CrossRef]
6. Tang, X.; Jiang, Z.; Jiang, S.; Wang, H.; He, Z.; Feng, J. Structure, burial, and gas accumulation mechanisms of lower Silurian Longmaxi Formation shale gas reservoirs in the Sichuan Basin (China) and its periphery. *AAPG Bull.* **2021**, *105*, 2425–2447. [CrossRef]
7. Xu, S.; Hao, F.; Zhang, Y.; Gou, Q. High-quality marine shale reservoir prediction in the lower Silurian Longmaxi Formation, Sichuan Basin, China. *Interpretation* **2020**, *8*, 1–42. [CrossRef]
8. Yu, W.; Sepehrnoori, K. Optimization of multiple hydraulically fractured horizontal wells in unconventional gas reservoirs. *J. Pet. Eng.* **2013**, *2013*, 1–16.
9. Peng, C.; Peng, J.; Chen, Y.; Zhang, H. Seismic prediction of sweet spots in the Da'anzhai shale play, Yuanba area, the Sichuan Basin. *Nat. Gas Ind. B* **2014**, *1*, 185–191.
10. Gao, J.; Wang, X.; He, S.; Guo, X.; Zhang, B.; Chen, X. Geochemical characteristics and source correlation of natural gas in Jurassic shales in the North Fuling area, Eastern Sichuan Basin, China. *J. Pet. Sci. Eng.* **2017**, *158*, 284–292. [CrossRef]
11. Shu, Z.; Zhou, L.; Li, X.; Liu, H.; Zeng, Y.; Xie, H.; Yao, M.; Wang, Y. Geological characteristics of gas condensate reservoirs and their exploration and development prospect in the Jurassic continental shale of the Dongyuemiao Member of Ziliujing Formation, Fuxing area, eastern Sichuan Basin. *Oil Gas Geol.* **2021**, *42*, 212–223.
12. He, W.; He, H.; Wang, Y.; Cui, B.; Meng, Q.; Guo, X.; Bai, X.; Wang, Y. Major breakthrough and significance of shale oil of the Jurassic Lianggaoshan Formation in Well Ping'an 1 in northeastern Sichuan Basin. *China Pet. Explor.* **2022**, *27*, 40–49.
13. Li, W.; Jiang, Z.; Qiu, H.; Zhu, D.; Gao, X.; Su, Z.; Yang, Z. Reservoir capacity evaluation of continental shale reservoirs in Da'anzhai Member of Lower Jurassic Ziliujing Formation in Northeast Sichuan. *China Energy Environ. Prot.* **2022**, *44*, 143–153.
14. Li, Y.; Feng, Y.; Liu, H.; Zhang, L.; Zhao, S. Geological characteristics and resource potential of lacustrine shale gas in the Sichuan Basin, SW China. *Pet. Explor. Dev.* **2013**, *40*, 454–460. [CrossRef]
15. Yang, Y.; Huang, D. Geological characteristics and new understandings of exploration and development of Jurassic lacustrine shale oil and gas in the Sichuan Basin. *J. Nat. Gas Ind.* **2019**, *39*, 22–33.
16. Qiu, Z.; Zou, C.N. Controlling factors on the formation and distribution of "sweet-spot areas" of marine gas shales in South China and a preliminary discussion on unconventional petroleum sedimentology. *J. Asian Earth Sci.* **2020**, *194*, 103989. [CrossRef]
17. Ma, Y.S.; Guo, X.S.; Guo, T.L.; Huang, R.; Cai, X.Y.; Li, G.X. The Puguang gas field: New giant discovery in the mature Sichuan Basin, southwest China. *AAPG Bull.* **2007**, *91*, 627–643. [CrossRef]
18. Qiu, Z.; He, J. Depositional environment changes and organic matter accumulation of Pliensbachian-Toarcian lacustrine shales in the Sichuan basin, SW China. *J. Asian Earth Sci.* **2022**, *232*, 1–16. [CrossRef]
19. Wei, L.; Shengfei, Q.; Guoyi, H.; Yanjie, G. Accumulation of water-soluble gas by degasification: One of important mechanisms of large gas accumulations in the Xujiahe Formation, Sichuan Basin. *Pet. Explor. Dev.* **2011**, *38*, 662–670. [CrossRef]
20. Gu, Z.; Yin, J.; Yuan, M.; Bo, D.; Liang, D.; Zhang, H.; Zhang, L. Accumulation conditions and exploration directions of natural gas in deep subsalt Sinian-Cambrian System in the eastern Sichuan Basin, SW China. *Pet. Explor. Dev.* **2015**, *42*, 152–166. [CrossRef]
21. Zhao, G.; Wang, Y.; Huang, B.; Dong, Y.; Li, S.; Zhang, G.; Yu, S. Geological reconstructions of the East Asian blocks: From the breakup of Rodinia to the assembly of Pangea. *Earth-Sci. Rev.* **2018**, *186*, 268–286. [CrossRef]
22. He, J.; Wang, J.; Milsch, H.; Qiu, Z.; Yu, Q. The characteristics and formation mechanism of a regional fault in shale strata: Insights from the Middle-Upper Yangtze, China. *Mar. Pet. Geol.* **2020**, *121*, 1–20. [CrossRef]
23. Creveling, J.R.; Finnegan, S.; Mitrovica, J.X.; Bergmann, K.D. Spatial variation in Late Ordovician glacioeustatic sea-level change. *Earth Planet. Sci. Lett.* **2018**, *496*, 1–9. [CrossRef]
24. Zou, C.; Qiu, Z.; Poulton, S.W.; Dong, D.; Wang, H.; Chen, D.; Lu, B.; Shi, Z.; Tao, H. Ocean euxinia and climate change" double whammy" drove the Late Ordovician mass extinction. *Geology* **2018**, *46*, 535–538. [CrossRef]
25. Liu, Y.J.; Huang, C.Y.; Zhou, Y.Q.; Lu, Y.C.; Ma, Q. The controlling factors of lacustrine shale lithofacies in the Upper Yangtze Platform (South China) using artificial neural networks. *Mar. Pet. Geol.* **2020**, *118*, 104350. [CrossRef]
26. Wang, X.Y.; Jin, Z.K.; Zhao, J.H.; Zhu, Y.X.; Hu, Z.Q.; Liu, G.X.; Jiang, T.; Wang, H.; Li, S.; Shi, S.T. Depositional environment and organic matter accumulation of Lower Jurassic nonmarine fine-grained deposits in the Yuanba Area, Sichuan Basin, SW China. *Mar. Pet. Geol.* **2020**, *116*, 104352. [CrossRef]
27. Li, Y.; He, D. Evolution of tectonic-depositional environment and prototype basins of the Early Jurassic in Sichuan Basin and adjacent areas. *Acta Pet. Sin.* **2014**, *35*, 219–232.

28. Jacob, H. Disperse solid bitumens as an indicator for migration and maturity in prospecting for oil and gas. *Erdoel Kohle Erdgas Petrochem.* **1985**, *38*, 365.

29. Zhu, D.; Jiang, Z.; Jiang, S.; Yang, W.; Song, Y.; Gao, Z.; Jiang, T.; Cao, X.; Li, W.; Zhang, Y. Water-bearing characteristics and their influences on the reservoir capacity in terrestrial shale reservoirs: A case study of the lower Jurassic Ziliujing Formation in the Northeast Sichuan Basin, China. *Mar. Pet. Geol.* **2021**, *123*, 1–16. [CrossRef]

30. Li, D.; Li, R.; Zhu, Z.; Wu, X.; Cheng, J.; Liu, F.; Zhao, B. Origin of organic matter and paleo-sedimentary environment reconstruction of the Triassic oil shale in Tongchuan City, southern Ordos Basin (China). *Fuel* **2017**, *208*, 223–235. [CrossRef]

31. Hou, H.; Shao, L.; Li, Y.; Lu, J.; Li, Z.; Wang, S.; Zhang, W.; Wen, H. Geochemistry, reservoir characterization and hydrocarbon generation potential of lacustrine shales: A case of YQ-1 well in the Yuqia Coalfield, northern Qaidam Basin, NW China. *Mar. Pet. Geol.* **2017**, *88*, 458–471. [CrossRef]

32. Xiong, F.; Jiang, Z.; Li, P.; Wang, X.; Bi, H.; Li, Y.; Wang, Z.; Amooie, M.A.; Soltanian, M.R.; Moortgat, J. Pore structure of transitional shales in the Ordos Basin, NW China: Effects of composition on gas storage capacity. *Fuel* **2017**, *206*, 504–515. [CrossRef]

33. Ma, Y.; Pan, Z.; Zhong, N.; Connell, L.D.; Down, D.I.; Lin, W.; Zhang, Y. Experimental study of anisotropic gas permeability and its relationship with fracture structure of Longmaxi Shales, Sichuan Basin, China. *Fuel* **2016**, *180*, 106–115. [CrossRef]

34. Liang, F.; Zhang, Q.; Lu, B.; Chen, P.; Su, C.; Zhang, Y.; Liu, Y. Pore Structure in Shale Tested by Low Pressure N2 Adsorption Experiments: Mechanism, Geological Control and Application. *Energies* **2022**, *15*, 4875. [CrossRef]

35. Wang, S.; Elsworth, D.; Liu, J. Permeability evolution in fractured coal: The roles of fracture geometry and water-content. *Int. J. Coal Geol.* **2011**, *87*, 13–25. [CrossRef]

36. Rist, U.; Günes, H. Qualitative and quantitative characterization of a jet and vortex actuator. In Proceedings of the 7th Ercoftac SIG33 Workshop, Genova, Italy, 16–18 October 2008; pp. 16–18.

37. Kumar, S.; Das, S.; Bastia, R.; Ojha, K. Mineralogical and morphological characterization of Older Cambay Shale from North Cambay Basin, India: Implication for shale oil/gas development. *Mar. Pet. Geol.* **2018**, *97*, 339–354. [CrossRef]

38. Li, W.; Yu, H.; Deng, H. Stratigraphic division and correlation and sedimentary characteristics of the Cambrian in central-southern Sichuan Basin. *Pet. Explor. Dev.* **2012**, *39*, 725–735. [CrossRef]

39. Chen, L.; Jiang, Z.; Liu, Q.; Jiang, S.; Liu, K.; Tan, J.; Gao, F. Mechanism of shale gas occurrence: Insights from comparative study on pore structures of marine and lacustrine shales. *Mar. Pet. Geol.* **2019**, *104*, 200–216. [CrossRef]

40. Hu, H.; Hao, F.; Lin, J.; Lu, Y.; Ma, Y.; Li, Q. Organic matter-hosted pore system in the Wufeng-Longmaxi (O3w-S11) shale, Jiaoshiba area, Eastern Sichuan Basin, China. *Int. J. Coal Geol.* **2017**, *173*, 40–50. [CrossRef]

41. Milliken, K.L.; Rudnicki, M.; Awwiller, D.N.; Zhang, T. Organic matter–hosted pore system, Marcellus formation (Devonian), Pennsylvania. *AAPG Bull.* **2013**, *97*, 177–200. [CrossRef]

42. Song, H.; Yu, M.; Zhu, W.; Wu, P.; Lou, Y.; Wang, Y.; Killough, J. Numerical investigation of gas flow rate in shale gas reservoirs with nanoporous media. *Int. J. Heat Mass Transf.* **2015**, *80*, 626–635. [CrossRef]

43. Zhang, L.; Li, B.; Jiang, S.; Xiao, D.; Lu, S.; Zhang, Y.; Gong, C.; Chen, L. Heterogeneity characterization of the lower Silurian Longmaxi marine shale in the Pengshui area, South China. *Int. J. Coal Geol.* **2018**, *195*, 250–266. [CrossRef]

44. Sing, K.S. Reporting physisorption data for gas/solid systems with special reference to the determination of surface area and porosity (Recommendations 1984). *Pure Appl. Chem.* **1985**, *57*, 603–619. [CrossRef]

45. Li, F.; Wang, M.; Liu, S.; Hao, Y. Pore characteristics and influencing factors of different types of shales. *Mar. Pet. Geol.* **2019**, *102*, 391–401. [CrossRef]

46. Yang, F.; Ning, Z.; Wang, Q.; Zhang, R.; Krooss, B.M. Pore structure characteristics of lower Silurian shales in the southern Sichuan Basin, China: Insights to pore development and gas storage mechanism. *Int. J. Coal Geol.* **2016**, *156*, 12–24. [CrossRef]

47. Borjigin, T.; Shen, B.; Yu, L.; Yang, Y.; Zhang, W.; Tao, C.; Xi, B.; Zhang, Q.; Bao, F.; Qin, J. Mechanisms of shale gas generation and accumulation in the Ordovician Wufeng-Longmaxi Formation, Sichuan Basin, SW China. *Pet. Explor. Dev.* **2017**, *44*, 69–78. [CrossRef]

48. Chen, C. Multiscale imaging, modeling, and principal component analysis of gas transport in shale reservoirs. *Fuel* **2016**, *182*, 761–770. [CrossRef]

49. Wang, X.; Gao, S.; Gao, C. Geological features of Mesozoic lacustrine shale gas in south of Ordos Basin, NW China. *Pet. Explor. Dev.* **2014**, *41*, 326–337. [CrossRef]

50. Guo, T. The Fuling Shale Gas Field—A highly productive Silurian gas shale with high thermal maturity and complex evolution history, southeastern Sichuan Basin, China. *Interpretation* **2015**, *3*, 25–34. [CrossRef]